lubricants

MDPI

Article

Optimization of Tribological Properties of 20CrMnTi Alloy with a Composite Bionic Texture and Graphene Coating for Gear Applications

Lexia Wei [1,2], Haowen Qin [1], Xuan Chen [1], Chenxi Wu [1], Shiyu Liu [1], Chaohua Wu [1,3,*] and Xiaoliang Shi [1]

[1] School of Mechanical and Electronic Engineering, Wuhan University of Technology, 122 Luoshi Road, Wuhan 430070, China; weilexia@wuling.com.cn (L.W.); 15527800651@163.com (H.Q.); 15727828819@163.com (X.C.); 18231663066@163.com (C.W.); 353123@whut.edu.cn (S.L.); sxl@whut.edu.cn (X.S.)

[2] Liuzhou Wuling New Energy Automobile Co., Ltd., Liuzhou 454616, China

[3] School of Intelligent Manufacturing, Xinjiang Vocational University, Urumqi 830039, China

[*] Correspondence: wuchaohua@whut.edu.cn; Tel./Fax: +86-27-87651793

Abstract

Surface-dominated failures such as micropitting, scuffing, and rolling contact fatigue remain critical challenges for 20CrMnTi gear steel under high-stress and poor lubrication conditions. Inspired by the composite bionic "checkerboard + dot-matrix dimple" architecture found in natural surfaces, this study aims to develop an optimized biomimetic texture combined with a graphene solid lubricant coating to enhance the tribological performance of 20CrMnTi alloy. Laser surface texturing was employed to fabricate the bionic pattern on 20CrMnTi substrates, followed by deposition of an oxysilane-graphene coating. Reciprocating ball-on-disc tribological tests were conducted under both dry friction and oil-lubricated conditions. The results showed that under dry friction, the optimized textured and coated specimen achieved an average friction coefficient of ~0.18, representing a ~62% reduction compared to the untextured surface (~0.47). Under oil lubrication, the friction coefficient was further reduced to ~0.10–0.11, demonstrating a synergistic effect among the texture, graphene coating, and lubricant. Wear volume decreased by over 70% under dry conditions. The dominant wear mechanism shifted from severe adhesive–abrasive–oxidative wear to mild adhesive and abrasive wear. These findings suggest that the proposed composite bionic texture combined with a graphene coating offers an effective strategy for improving the tribological durability of 20CrMnTi gear.

Keywords: 20CrMnTi; composite bionic texture; graphene coating; tribological properties; laser surface texturing; wear mechanism; lubrication

Check for updates

Received: 2 July 2026
Revised: 26 July 2026
Accepted: 27 July 2026
Published: 31 July 2026

Copyright: © 2026 by the authors. Licensee MDPI, Basel, Switzerland. This article is an open access article distributed under the terms and conditions of the Creative Commons Attribution (CC BY) license.

1. Introduction

The surface of a component serves as the primary interface between the bulk material and its operating environment, mediating contact stress, lubricant interaction, and debris generation and ultimately determining the component's service life [1,2]. For high-load power-transmission parts such as gears, surface design rather than bulk composition often dictates the failure mode, making surface engineering a critical lever for performance enhancement [3–5].

Gear steels, particularly 20CrMnTi [1,3,6], are extensively employed in critical power transmission components such as automotive transmissions, wind turbine gearboxes, and heavy-duty mining equipment, owing to their excellent core toughness, high hardenability, and good fatigue resistance after carburizing and quenching [1,3,4]. However, under conditions of high contact stress, cyclic loading, and inadequate lubrication—common in demanding operational environments—these components remain susceptible to surface-dominated failures [7,8]. These include micropitting, scuffing, and rolling contact fatigue (RCF), which are primarily driven by excessive friction, subsurface stress concentrations, and localized thermal softening [8–11]. Consequently, enhancing the surface tribological properties of 20CrMnTi without compromising its bulk mechanical integrity and fatigue strength presents a persistent challenge [12–14].

Traditional surface enhancement strategies for 20CrMnTi have focused on increasing surface hardness and fatigue resistance. Carburizing and quenching remain the industrial baseline [1,3], while supplementary treatments such as deep cryogenic treatment [12], ultrasonic shot peening [13], and PVD coatings (CrN, TiN, DLC) [11,12] have been actively explored to further suppress wear and RCF. However, these approaches can inadvertently increase brittleness, promote coating/substrate crack initiation under heavy cyclic loads, or offer limited benefit under starved lubrication [15,16]. Laser surface texturing (LST) has emerged as a promising alternative for creating micro-reservoirs to retain lubricant and capture wear debris [17–19]. Nevertheless, simplistic textures like uniform dimple arrays can act as stress raisers, potentially accelerating RCF crack nucleation under high Hertzian contact stresses [11,20]. This highlights the inherent trade-off in conventional approaches and underscores the need for a more integrated surface design strategy that simultaneously manages friction, stress, and thermal loads.

Bioinspired surface design offers a paradigm shift by mimicking nature's multifunctional structures [21]. Beyond single-feature prototypes like lotus leaves or shark skin, composite structures integrating macro-scale patterning with micro-scale topography show greater potential for synergistic functionality [22–24]. Inspired by this principle, a "checkerboard + dot-matrix dimple" composite bionic structure is conceptualized. This design merges the macro-partitioning concept, analogous to the scale patterns on reptile skin which manage functional zoning [25,26], with a micro-scale array of dimples reminiscent of the lubricant-retaining pores in joint cartilage or the drag-reducing denticles of shark skin [21–23]. The "checkerboard" layout aims to create distinct zones for stress redistribution and debris management, while the "dot-matrix dimples" within each zone function as micro-reservoirs and traps.

Related research provides a foundation for such multifunctional textures. For instance, textured surfaces mimicking natural patterns have demonstrated success in friction reduction for ceramics and polymers [22,27]. Furthermore, the integration of solid lubricants like graphene—a two-dimensional material renowned for its exceptional lubricity, high thermal conductivity, and mechanical strength—into surface textures has shown promise in forming adaptive lubricating films [28]. However, most existing studies focus on non-ferrous substrates or simplified contact conditions. A significant research gap remains in the development and holistic assessment of such composite bioinspired textures, synergized with advanced solid lubricants like graphene, on high-strength gear steels like 20CrMnTi [29].

To address this gap, this study pioneers a composite biomimetic surface texture for 20CrMnTi, inspired by the "checkerboard + dot-matrix dimple" architecture and enhanced with a graphene coating, which has not been reported. Laser surface texturing is employed to fabricate this optimized design on 20CrMnTi substrates. This study, therefore, pioneers such a system, aiming to achieve three concurrent functionalities: (i) friction control via the graphene solid lubricant and micro-dimples; (ii) wear debris entrapment within the dimple arrays to mitigate three-body abrasion; and (iii) stress field modulation through the checkerboard partitioning to delay fatigue crack initiation. This study conducted tribological tests under dry friction and oil lubrication conditions to reveal the friction reduction and wear resistance mechanism of the graphene-coated-composite bionic texture.

2. Materials and Methods

2.1. Materials

The experimental materials comprised 20CrMnTi steel plates, which are used to manufacture the rear axle gears of new energy vehicles, and graphene coating. The graphene coating contains components such as graphene and oxygen silanes. For experimental processing, 20CrMnTi plates were sectioned into 15 × 15 × 10 mm^3 specimens using wire electrical discharge machining (EDM). The contact surfaces were precision-machined to replicate real-world operating surface conditions.

Table 1 shows the chemical content of 20CrMnTi and Figure 1 shows its actual engineering application environment.

Table 1. Chemical content of 20CrMnTi (wt.%).

Element	C	Si	Mn	Cr	Ti	Ni	Fe	Else
Weight percentage	0.12	0.23	1.02	1.26	0.08	0.15	97.03	≤0.11

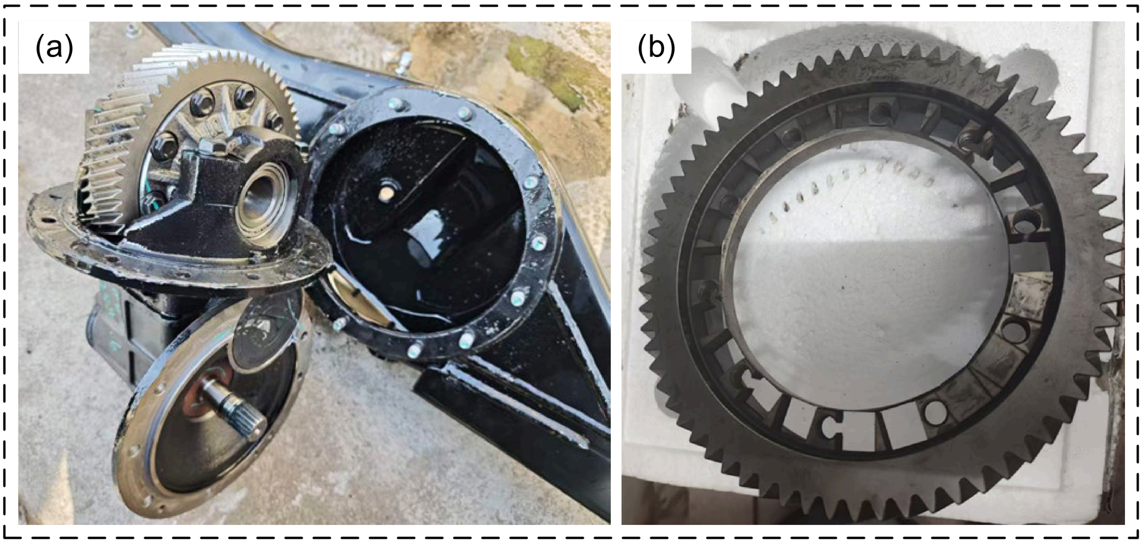

Figure 1. The rear axle of new energy vehicles (**a**) and gears on the rear axle (**b**).

2.2. Fabrication of Bionic Texture

Laser ablation (Figure 2) was employed to fabricate textured specimens. Specimens were ultrasonically cleaned in acetone and ethanol sequentially for 10 min each, then dried with nitrogen gas before texturing. The laser parameters were optimized through preliminary trials: 46% laser power (13.8 W of 30 W), 1000 mm/s scan speed, 32 passes, and 200 μm ablation depth. These settings produced clean micro-grooves and dimples with minimal heat-affected zones; lower power (<40%) yielded insufficient depth, while higher power (>55%) caused excessive melting and burr formation. Post-texturing, surfaces underwent sequential mechanical grinding with 600-, 1000-, and 1200-grit metallographic abrasive papers to remove oxides, burrs, and macro-scale scratches. Ultrasonic cleaning in 95 vol% ethanol was conducted for 15 min, followed by surface ethanol removal via compressed air purging. Specimens were subsequently stored in anti-static sealed bags.

https://doi.org/10.3390/lubricants14080299

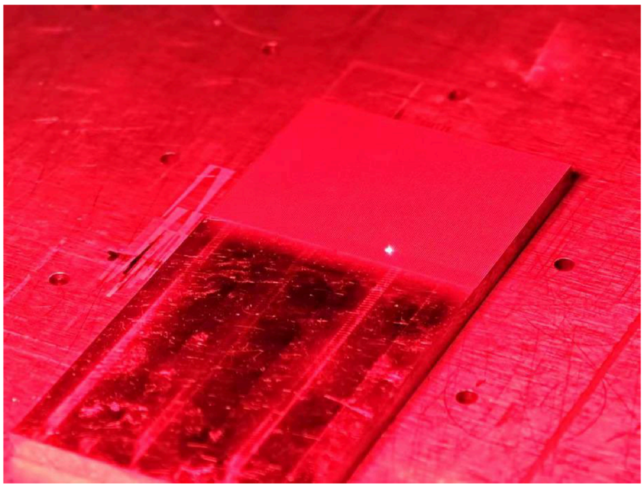

Figure 2. Laser ablation processing.

In this experiment, the samples were divided into four groups: W, A, B, and C, with each having different surface texture parameters, as shown in Table 2. l (mm) represents the spacing of the groove texture, s (mm) represents the width of the groove texture, and d (mm) represents the diameter of the circular depression texture. Group W represents the non-textured 20CrMnTi sample, while groups A, B, and C represent 20CrMnTi samples with different groove parameters that include texture, as shown in Figure 3.

Table 2. Parameter range of bionic texture.

Texture Parameters	l/mm	s/mm	d/mm	Area Percentage%
W	0	0	0	0%
A	1.84	0.35	0.46	29.01%
B	1.15	0.58	0.46	59.14%
C	1.38	0.35	0.46	39.55%

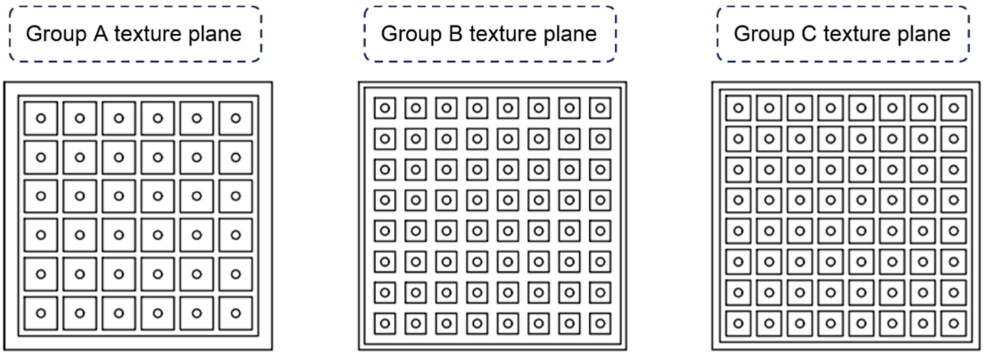

Figure 3. Layout and appearance of each organizational level.

2.3. Graphene Coating Deposition

A syringe was used to draw the liquid graphene–organosilicon coating, which was then evenly spread across the textured surface of the samples. The blocks were subsequently clamped with a hot-pressing mold and transferred into a vacuum infiltration furnace. Heating was conducted at 180 °C for 2.5 h under a vacuum of 0.1 Pa. Figure 4 shows the whole process of the coating preparation of the blocks. After naturally cooling to room temperature, the samples were finely ground and polished, yielding TC4-based bio-inspired texture–graphene coating material specimens. Figure 5 shows the microscopic appearance of the graphene raw material.

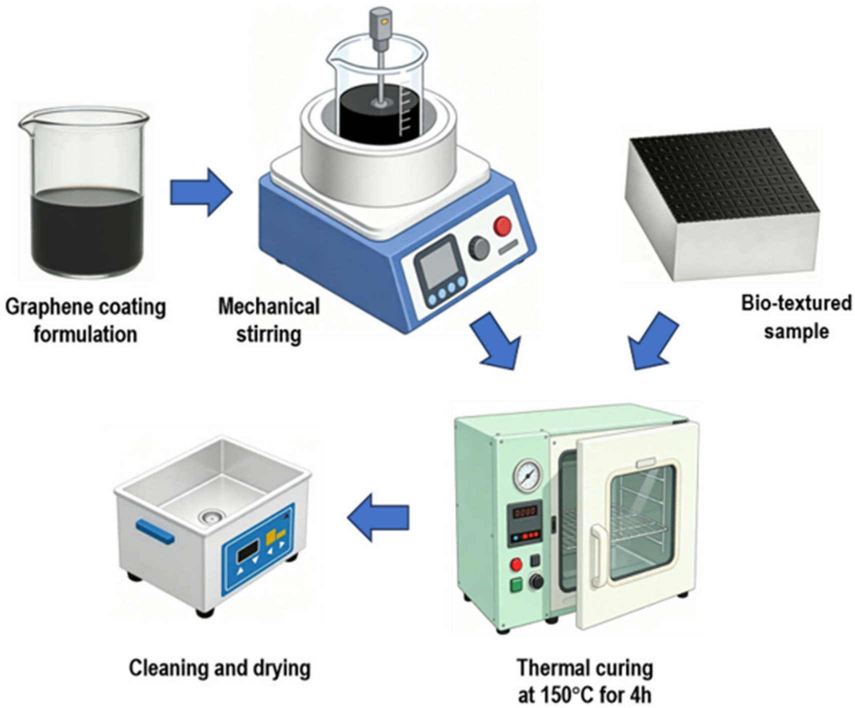

Figure 4. Preparation process of graphene composite coating.

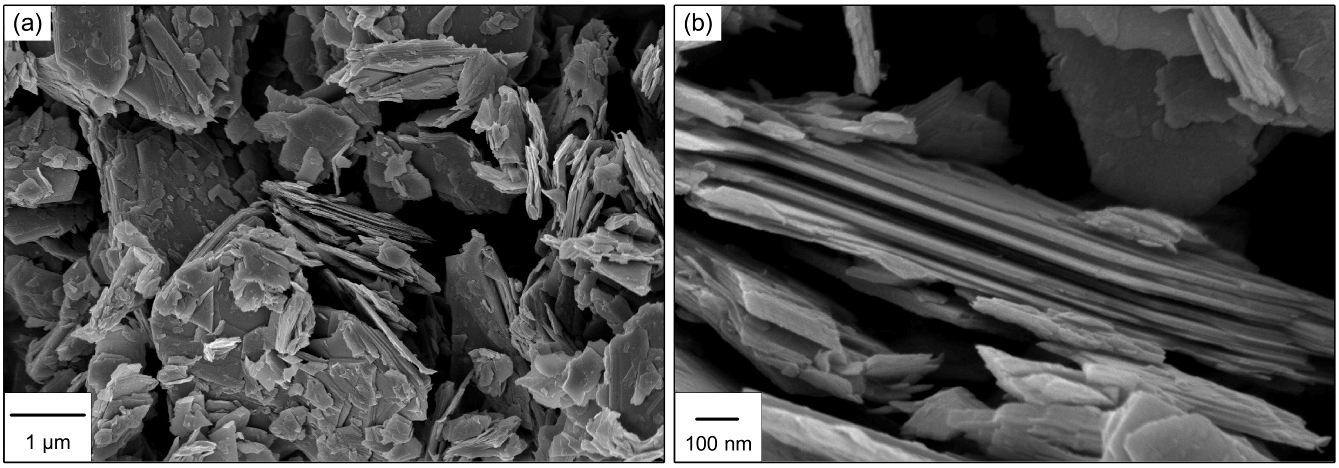

Figure 5. Microscopic morphology of the graphene raw material magnified 10,000 times (**a**) and 60,000 times (**b**).

2.4. Tribological Testing

To investigate the coupling effects of the composite bionic texture and graphene solid lubricant on the tribological performance of the 20CrMnTi alloy, comparative friction and wear tests were conducted on untextured, textured, and textured-with-graphene specimens. All experiments were performed using an MFT-5000 multifunctional tribometer (Rtec, San Jose, CA, USA) (Figure 6) in a ball-on-disk reciprocating configuration, with AISI 52100 steel balls (Ø 6.35 mm) serving as the counterface material. The key testing parameters for dry friction conditions were as follows: an ambient temperature of 20–25 °C, a relative humidity of 40–60%, a normal load of 30 N, a stroke length of 8 mm, a sliding frequency of 2 Hz, and a test duration of 30 min. Each test condition was repeated three times to ensure statistical reliability, and the mean values of the coefficient of friction (COF) are reported. The COF data were recorded in real time by the tribometer's integrated system.

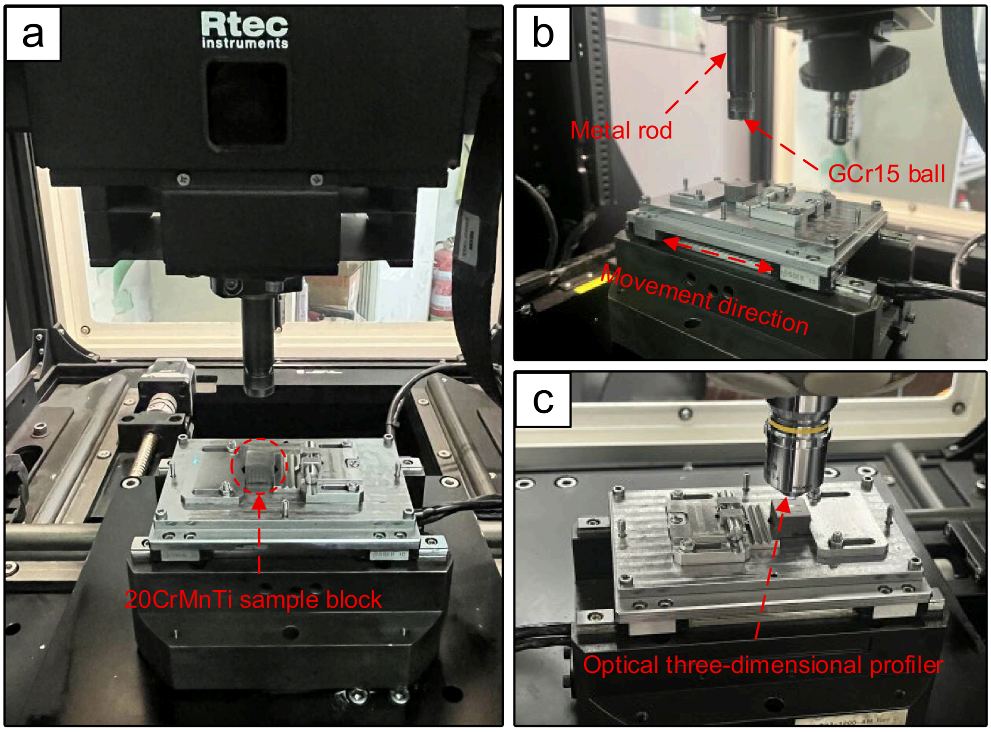

Figure 6. Friction and wear testing machine (**a**), reciprocating friction testing module (**b**) and white-light interference module (**c**).

For oil-lubrication studies, a bath of GL-5 heavy-duty vehicle gear oil was applied to fully immerse the contact zone and the textured surface, while all other kinematic and loading parameters remained identical to those used in the dry friction tests. This approach ensured a direct and meaningful comparison of the surface performance under different lubrication regimes.

Following testing, the worn surfaces were characterized using an ST-500 optical profilometer, as shown in Figure 6c, to obtain three-dimensional topography maps. Multiple cross-sectional profiles were extracted from these reconstructed surfaces. To ensure accuracy, a standardized measurement protocol was implemented: profilometric scans were performed at four equidistant locations along the sliding track, with each location measured three times. The data for each sampling point were subsequently averaged. The cumulative wear volume was finally calculated by integrating the cross-sectional area of the wear track over the total reciprocating sliding distance, consistent with the principles of Archard wear analysis:

$$V = \sum_{i=1}^{n} A_i \times L$$

where V represents the cumulative wear volume (mm^3), A_i denotes the cross-sectional area at measurement point i (mm^2), and L signifies the total sliding distance (m) [30,31].

2.5. Characterization Methods

All characterizations were performed using the following instruments: optical profilometer (ST-500, Nanovea, San Jose, CA, USA) and field-emission SEM (Zeiss Gemini 300, Jena, Germany) equipped with EDS (Oxford X-Max, Oxford, UK).

3. Results and Discussions

3.1. White-Light Interference Analysis

Post-testing, the worn surfaces under dry friction conditions were characterized using white light interferometry to evaluate the micro-topographical evolution and wear mechanisms. As shown in Figure 7, the 3D surface topography maps and corresponding cross-sectional profiles reveal distinct differences among the specimens. The untextured 20CrMnTi sample exhibits a relatively smooth surface interrupted by deep abrasive grooves, characteristic of severe adhesive wear and material transfer. In contrast, the specimen with only the bionic texture shows a patterned landscape where the 'checkerboard + dot-matrix' depressions serve as reservoirs for wear debris, preventing the formation of large-scale destructive scratches and maintaining overall surface integrity. Most notably, the sample incorporating both the bionic texture and graphene coating demonstrates a significantly milder wear track. The graphene lubricant fills the micro-dimples and covers the peaks, facilitating the formation of a stable tribo-film that reduces direct metal-to-metal contact. This analysis confirms that the composite bionic structure synergistically enhances load distribution and lubrication retention, effectively mitigating plowing and abrasive wear under harsh dry friction conditions.

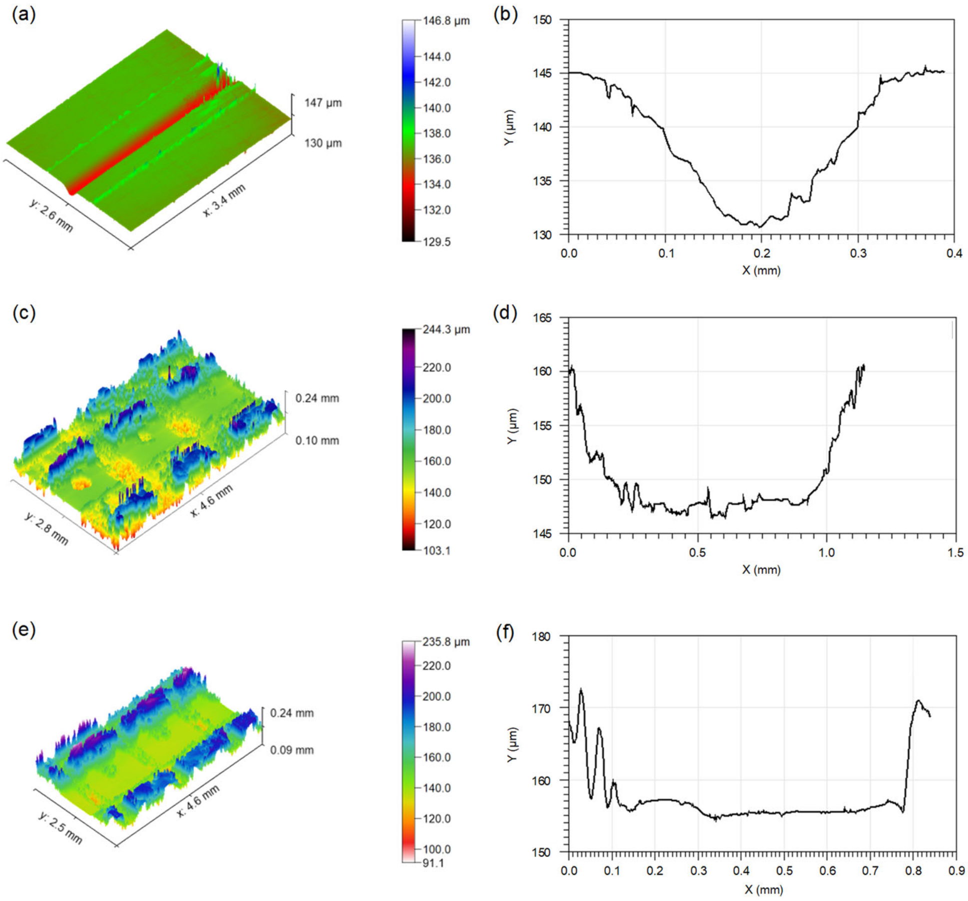

Figure 7. Three-dimensional topography maps (**a**,**c**,**e**) and two-dimensional cross-sectional view (**b**,**d**,**f**) of the grinding marks.

3.2. Friction Coefficient Analysis

Under dry reciprocating sliding conditions at a normal load of 30 N, a frequency of 2 Hz, and a test duration of 30 min, the untextured 20CrMnTi specimen showed the highest average friction coefficient, approximately 0.47 in Figure 8b. In contrast, the specimens with square-grid grooves, circular dimples at the grid centers, and a sintered oxysilane–graphene coating exhibited markedly reduced friction coefficients. Among them, group C showed the lowest value, approximately 0.18. This result indicates that the hybrid surface texture and oxysilane–graphene coating can effectively improve the interfacial lubrication behavior of 20CrMnTi steel under dry sliding conditions. The continuous square-grid grooves can redistribute the contact stress, reduce adhesive contact, and interrupt the propagation of plowing grooves, while the circular dimples serve as debris-trapping reservoirs, thereby suppressing three-body abrasive wear. In addition, the grooves and dimples provide effective mechanical anchoring sites for the oxysilane–graphene coating, improving coating retention during reciprocating shear. During sliding, graphene nanosheets can be preferentially oriented and spread over the contact interface, forming a low-shear-strength transfer film, whereas the oxysilane component contributes to enhanced interfacial adhesion between the coating and the steel substrate, thereby delaying coating delamination. For the three textured groups, the main parameters affecting friction are the groove width and spacing, dimple geometry, texture area fraction, and coating retention. An excessively dense texture can reduce the effective load-bearing area and increase local stress concentration, whereas an excessively sparse texture provides insufficient coating storage and debris capture. Compared with groups A and B, the texture design of group C appeared to provide a more favorable balance among coating storage, debris entrapment, and load-bearing area. Therefore, its superior performance should be attributed to the combined effect of texture geometry and coating stability rather than to a single structural parameter. Consequently, a more stable lubricating transfer film can be maintained, leading to reduced adhesive and abrasive wear contributions and, therefore, the lowest average friction coefficient.

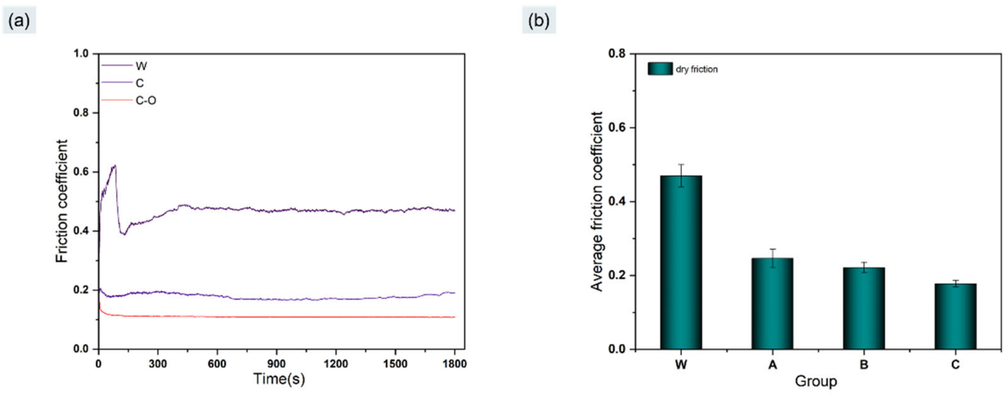

Figure 8. Comparison of dry friction coefficients in group W and group C with oil (C-O)-lubricated friction coefficients (**a**), an average friction coefficient under dry friction conditions in group W, group A, group B, and group C (**b**).

The evolution of the friction coefficient of 20CrMnTi specimens with different surface conditions during reciprocating sliding tests is shown in Figure 8a. The untreated specimen (group W) exhibited the highest friction coefficient and pronounced fluctuations during the initial stage under dry sliding conditions. The friction coefficient increased rapidly at the beginning of the test, reached a transient peak, and then gradually stabilized at approximately 0.46–0.48 after the running-in stage. This behavior indicates that severe direct contact occurred at the tribological interface of the untextured surface, where asperity shearing, adhesive interaction, and plowing contributed to high friction resistance and relatively unstable sliding. In contrast, group C, consisting of a square-grid groove/circular-dimple composite texture coated with sintered siloxane-functionalized graphene, showed a markedly reduced friction coefficient under dry sliding, with a steady-state value of approximately 0.17–0.19 and smaller fluctuations. This result suggests that the surface texture reduced the real contact area to some extent and provided reservoirs for wear debris, thereby mitigating three-body abrasive wear. Meanwhile, the siloxane-functionalized graphene coating may have formed a low-shear-strength lubricating or transfer film at the sliding interface, reducing the interfacial shear resistance of the friction pair. At the fixed test conditions used here, the observed differences among groups W, A, B, and C are, therefore, mainly related to texture dimensions, texture density, and the ability of each texture to retain and continuously supply the coating. Under oil-lubricated conditions, the C-O group exhibited the lowest and most stable friction coefficient, remaining at approximately 0.10–0.11 throughout most of the test. This improvement can be attributed to the oil-storage and oil-supply capacity of the composite texture, which helps maintain the continuity of the lubricating film, while the graphene coating provides additional solid-lubricating protection under boundary lubrication conditions. Accordingly, the further decrease in friction for C-O is controlled by the combined oil-retention capacity of the grid–dimple texture and the supplementary protection of the graphene transfer film. Overall, the combination of composite surface texturing and the siloxane-functionalized graphene coating effectively reduced the friction coefficient of the 20CrMnTi/GCr15 friction pair and promoted a transition from an unstable high-friction regime to a stable low-friction sliding state. The further reduction in friction under oil lubrication demonstrates the synergistic effect among the surface texture, graphene-based coating, and lubricating medium.

3.3. Microscopic Characterization Analysis

In Figure 9, for the untextured 20CrMnTi specimen, after reciprocating sliding against the GCr15 counter ball under a normal load of 30 N at 2 Hz for 30 min, pronounced parallel furrows, accumulated wear debris, and localized material transfer were observed within the wear track. These features indicate that micro-cutting, plowing, and adhesive tearing occurred during the sliding process. The EDS elemental maps show that Fe was the dominant element in the worn region, while Cr, Mn, and Si were relatively uniformly distributed. In contrast, O was clearly enriched in the wear track and debris-accumulated regions, suggesting oxidation of freshly exposed metallic surfaces and the formation of oxide debris during friction. On the GCr15 counter ball, a wear scar, shallow furrows, and a localized transfer layer were observed. The adhered material near the edge of the wear scar indicates that material from the 20CrMnTi specimen was transferred to the counter ball surface under interfacial shear. Based on the SEM and EDS results, the wear mechanism of the untextured specimen can be attributed to the combined action of adhesive wear, abrasive wear, and oxidative wear. In particular, debris generated by adhesive delamination remained within the contact interface and further participated in three-body abrasion, thereby aggravating the plowing damage on the worn surface.

For group C with continuous square grid grooves, central circular dimples, and a sintered oxysilane–graphene coating, the wear track formed under the same load, frequency, and sliding duration was generally smoother than that of the untextured specimen. In Figure 10a,b, only shallow furrows, a small amount of wear debris, and limited material transfer were locally observed, indicating that the surface texture and coating effectively alleviated adhesive tearing and abrasive plowing at the steel/steel contact interface. In Figure 10e, the EDS results revealed that, in addition to the Fe signal from the steel substrate, C, Si, and O were still detected in the worn region, indicating that the oxysilane–graphene coating or its tribochemical products partially remained after sliding and contributed to the formation of a C-Si-O-containing composite tribofilm. In Figure 10c,d, the wear scar on the GCr15 counter ball was relatively smooth, with a localized transfer layer originating from the specimen surface. Meanwhile, C, Si, and O were also detected on the ball surface, confirming the transfer of coating constituents and tribochemical products to the GCr15 counterface and the formation of a transfer film with reduced shear resistance in Figure 10f. Compared with the untextured specimen, the synergistic effect between the surface texture and the oxysilane–graphene coating reduced direct metal-to-metal contact within the tribopair. The continuous grooves and circular dimples could accommodate part of the wear debris, thereby weakening the repeated cutting action of debris within the contact zone. In addition, the graphene-related carbonaceous phase and siloxane-derived species were beneficial for the formation of low-shear transfer films and tribofilms, which reduced adhesive tearing, plowing wear, and interfacial damage caused by unstable oxide debris. The SEM results indicate that the spherical abrasion marks of GCr15 were smoother and had less debris. According to the EDS results, comparing the specific element distribution on the wear marks in Tables 3–6, the mutual transfer between the abrasive balls and the matrix material of the sample block was reduced. The abrasive debris mainly consisted of a combination of a small amount of debris and the peeled-off components of the solid lubricating coating, which continuously replenished the solid lubricant and promoted the formation of the friction film on the friction area. Under this effect, the grooves of the abrasive balls were shallower and more evenly distributed, and the wear pattern became more consistent. The damage of the paired balls was reduced, and their working condition also tended to improve.

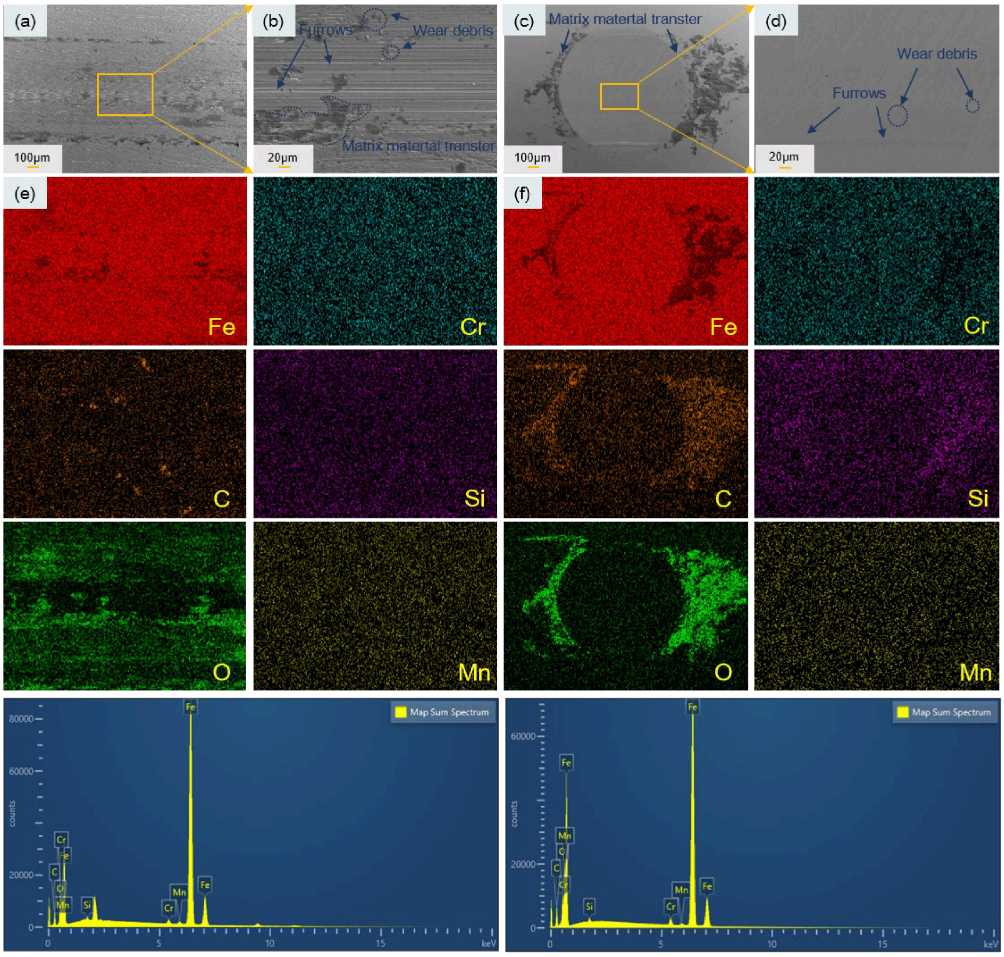

Figure 9. SEM and EDS characterization analysis of the group W sample block's worn surface (**a**,**b**,**e**), SEM and EDS characterization analysis of the ball milling marks corresponding to GCr15 for the group W sample blocks (**c**,**d**,**f**).

Table 3. Chemical content of the group W sample block's worn surface.

Element	C	O	Si	Cr	Mn	Fe
Wt%	7.43	0.49	0.22	1.44	0.40	90.02
Wt% Sigma	0.13	0.04	0.02	0.03	0.03	0.14
Atomic%	26.86	1.33	0.34	1.20	0.32	69.95

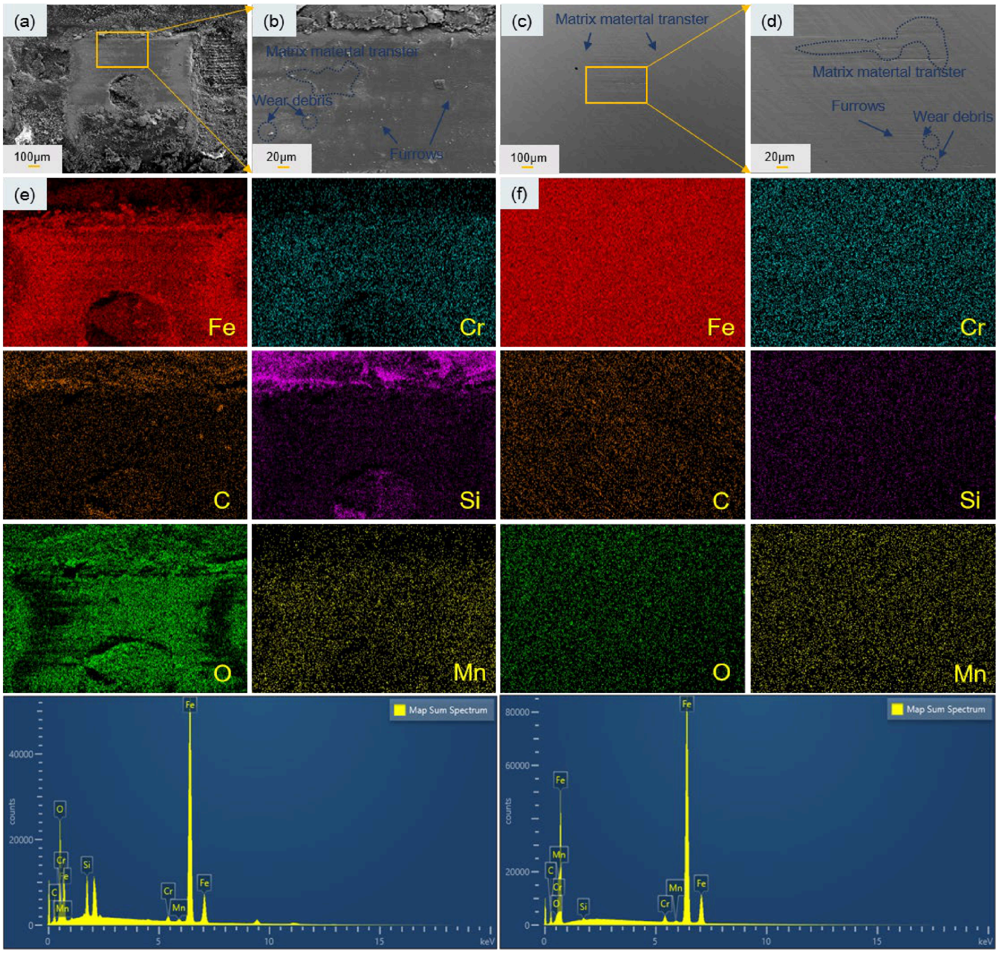

Figure 10. SEM and EDS characterization analysis of the group C sample block's worn surface (**a**,**b**,**e**), SEM and EDS characterization analysis of the ball milling marks corresponding to GCr15 for the group C sample blocks (**c**,**d**,**f**).

Table 4. Chemical content of the ball milling marks for the group W sample blocks.

Element	C	O	Si	Cr	Mn	Fe
Wt%	13.35	13.63	3.21	0.87	0.54	68.39
Wt% Sigma	0.17	0.09	0.04	0.03	0.04	0.16
Atomic%	33.38	25.60	3.44	0.50	0.29	36.79

Table 5. Chemical content of the group C sample block's worn surface.

Element	C	O	Si	Cr	Mn	Fe
Wt%	19.07	10.15	6.11	0.67	0.45	63.57
Wt% Sigma	0.19	0.09	0.05	0.03	0.04	0.17
Atomic%	44.12	17.63	6.04	0.36	0.23	31.63

Table 6. Chemical content of the ball milling marks for the group C sample blocks.

Element	C	O	Si	Cr	Mn	Fe
Wt%	11.45	3.92	0.39	1.36	0.32	82.56
Wt% Sigma	0.15	0.07	0.02	0.03	0.04	0.16
Atomic%	35.02	9.00	0.51	0.96	0.21	54.30

https://doi.org/10.3390/lubricants14080299

Under oil-lubricated conditions, group C-O exhibited a further improved tribological response. The SEM observations in Figure 11a,b showed that the wear track became smoother, and no obvious large-area delamination, deep furrows, or severe adhesive tearing was detected. Only a few fine scratches, localized wear debris, and limited material transfer were present, indicating that the introduction of lubricating oil further reduced direct contact between the tribopair surfaces. The EDS results in Figure 11e showed that Fe, C, Si, and O were still detected in the worn region. The C signal may have originated from the residual graphene coating, carbonaceous transfer film, and friction-induced products derived from the lubricating oil, whereas Si and O were associated with the residual oxysilane coating, Si–O structures, and slight oxidation products. The specific element proportions of the wear marks are shown in Table 7. The wear scar on the GCr15 counter ball in Figure 11c,d was relatively smooth, with only localized transfer layers and shallow furrows. Moreover, C, Si, and O were also detected on the ball surface in Figure 11f, indicating that coating constituents, tribochemical products, and oil-related products from the specimen surface jointly contributed to the formation of a transfer film on the counterface. The specific element proportions of the wear marks are shown in Table 8. Compared with the textured and coated specimen tested under dry sliding, the continuous square grid grooves and circular dimples under oil-lubricated conditions not only trapped wear debris but also served as oil reservoirs and supply units, helping to maintain the stability of a local boundary or mixed lubrication film. Meanwhile, the C–Si–O composite film derived from the oxysilane–graphene coating, together with the lubricating oil film, reduced the interfacial shear strength and suppressed the repeated cutting action of debris in the contact region. Therefore, under oil-lubricated conditions, the wear of this textured coating system was mainly characterized by mild adhesive wear, mild abrasive wear, and controlled oxidative wear under boundary/mixed lubrication, and its resistance to adhesive wear, abrasive wear, and counterface damage was further improved compared with group W.

Table 7. Chemical content of the group C-O sample block's worn surface.

Element	C	O	Si	Cr	Mn	Fe
Wt%	8.32	0.54	0.23	1.45	0.35	89.11
Wt% Sigma	0.14	0.05	0.02	0.03	0.03	0.15
Atomic%	29.29	1.43	0.35	0.18	0.27	67.48

Table 8. Chemical content of the ball milling marks for the group C-O sample blocks.

Element	C	O	Si	Cr	Mn	Fe
Wt%	7.43	0.49	0.22	1.44	0.40	90.02
Wt% Sigma	0.13	0.04	0.02	0.03	0.03	0.14
Atomic%	26.86	1.33	0.34	1.20	0.32	69.95

In summary, the untextured 20CrMnTi specimen mainly underwent a coupled adhesive, abrasive, and oxidative wear process during reciprocating dry sliding, as evidenced by deep plowing grooves, debris accumulation, material transfer, and oxygen enrichment. In contrast, the synergistic combination of continuous square-grid grooves, central circular dimples, and the oxysilane–graphene coating resulted in a much smoother wear track, with markedly suppressed plowing and adhesive tearing. The grooves and dimples contributed to stress regulation, wear-debris entrapment, and lubricant storage, while the graphene-derived carbonaceous phase and oxysilane-derived Si–O species promoted the formation of a low-shear-strength C–Si–O composite tribofilm and transfer film at the 20CrMnTi/GCr15 tribological interface. This structure-confined tribofilm reduced direct metal-to-metal contact and weakened the cutting action of third-body debris, thereby transforming the dominant wear mode from severe adhesive–abrasive–oxidative wear to controlled mild adhesive wear, slight abrasive wear, and moderate oxidative wear. Under oil-lubricated conditions, the composite texture further acted as a micro-reservoir and lubricant-supply network, improving the stability of the boundary/mixed lubrication film and highlighting the multiscale synergistic friction-reduction and wear-resistance mechanism among the texture, coating, and lubricant medium.

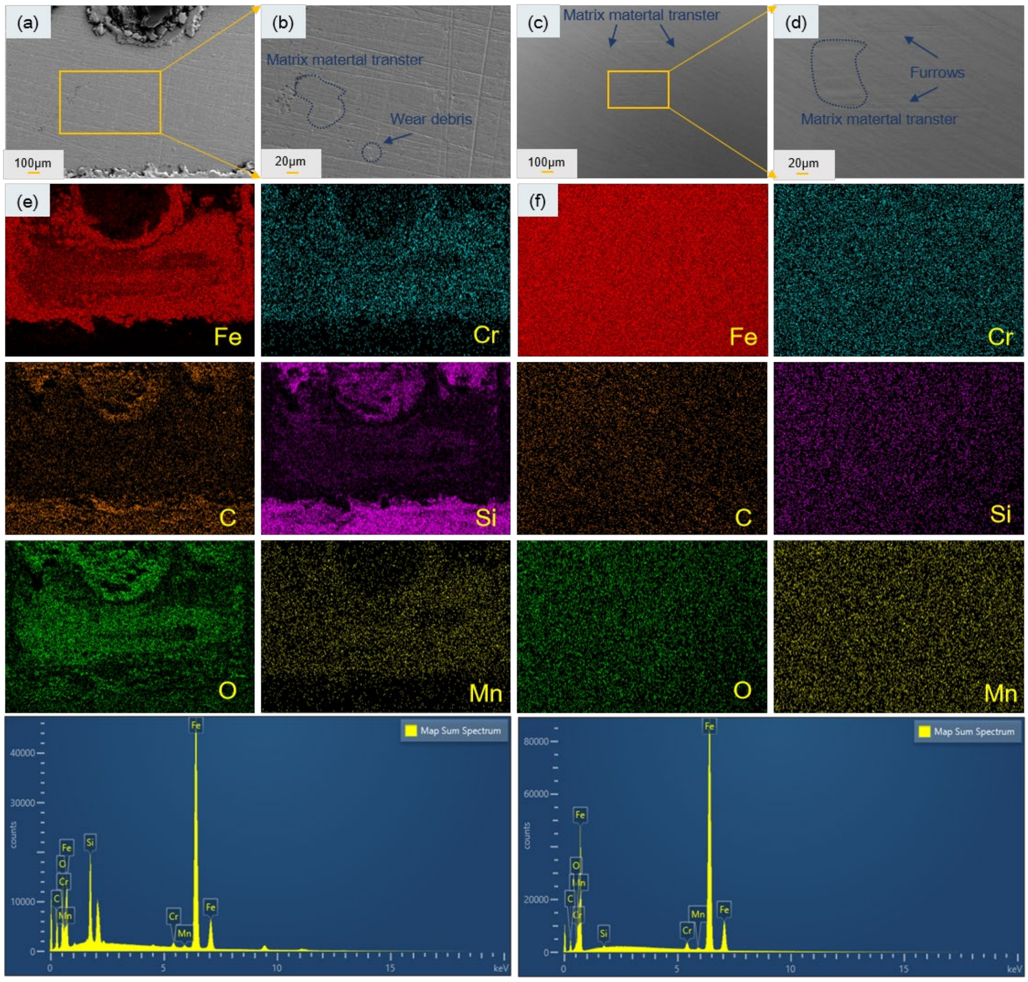

Figure 11. SEM and EDS characterization analysis of the group C-O sample block's worn surface (**a**,**b**,**e**), SEM and EDS characterization analysis of the ball milling marks corresponding to GCr15 for the group C-O sample blocks (**c**,**d**,**f**).

To contextualize the performance of the proposed strategy, Table 9 compares the friction coefficient and wear characteristics of the optimized group C specimen with representative surface engineering approaches reported in the recent literature for gear steels or similar alloys. Conventional laser surface texturing with simple dimple arrays typically reduces the friction coefficient to 0.3–0.4 under dry sliding [15,32], while single-layer PVD coatings such as CrN or DLC achieve values around 0.2–0.3 [11,12]. Simpler bio-inspired textures (e.g., groove-only or pit-only patterns) on steel substrates generally yield friction coefficients above 0.25 under dry conditions [23,33]. In contrast, the present composite "checkerboard + dot-matrix" bionic texture combined with an oxysilane–graphene coating achieved a friction coefficient as low as ~0.18 under dry friction and ~0.10–0.11 under oil lubrication, representing a ~62% and ~77% reduction, respectively, relative to the untextured surface. Furthermore, the wear volume was reduced by over 70%. These comparisons highlight the synergistic advantage of the multiscale texture design and solid lubricant coating, which collectively outperformed many existing single-strategy approaches. Thus, the proposed system offers a competitive solution for enhancing the tribological durability of 20CrMnTi gear components under demanding operating conditions.

Table 9. Comparison of friction coefficients.

Strategy	Substrate	Friction Coefficient (Dry)	Reference
LST	Steel	0.30–0.40	[34]
PVD CrN/DLC coating	Steel	0.20–0.30	[35]
Groove-only bio-texture	Steel	0.28–0.35	[36]
This work (Group C)	20CrMoTi	0.18 (dry) 0.10 (oil)	[37]

4. Summary and Outlooks

In this study, a composite bionic texture consisting of continuous square-grid grooves and central circular dimples was successfully fabricated on 20CrMnTi steel via laser surface texturing, followed by the deposition of an oxysilane–graphene coating. The main conclusions are systematically summarized as follows:

(1) The coupled texture/coating system significantly improved the tribological performance of the 20CrMnTi/GCr15 friction pair. Under dry sliding, the optimized group C specimen achieved an average friction coefficient of ~0.18, representing a ~62% reduction compared to the untextured surface (~0.47). Under oil lubrication, the friction coefficient was further reduced to ~0.10–0.11, demonstrating a clear synergistic effect among the composite texture, graphene coating, and lubricating oil.

(2) The enhanced tribological behavior is attributed to the multifunctional roles of the bionic texture and coating: the square-grid grooves redistributed contact stress and interrupted plowing propagation; the circular dimples served as reservoirs for wear debris and lubricant; and the oxysilane–graphene coating promoted the formation of low-shear C-Si-O-containing tribofilms and transfer films, reducing direct metal-to-metal contact.

(3) SEM, EDS, and 3D profilometry confirmed that the dominant wear mechanism shifted from severe adhesive–abrasive–oxidative wear to mild adhesive and abrasive wear, with wear volume reduced by over 70%.

(4) Potential applications: The proposed composite bionic texture combined with an oxysilane–graphene coating offers a promising and scalable surface engineering strategy for improving the tribological durability of 20CrMnTi gear components used in automotive transmissions, wind turbine gearboxes, and heavy-duty mining equipment, particularly under starved lubrication or boundary lubrication conditions. This approach can potentially extend component service life, reduce maintenance costs, and improve energy efficiency in power transmission systems.

Author Contributions: L.W.: Writing—Original Draft, Methodology, Investigation, Conceptualization, Data Curation, Software. H.Q.: Writing—Review and Editing. X.C.: Validation, Data Curation. C.W. (Chenxi Wu): Methodology, Conceptualization. S.L.: Methodology, Data Curation. C.W. (Chaohua Wu): Writing—Review and Editing, Software, Methodology, Resources. X.S.: Supervision, Resources, Conceptualization. All authors have read and agreed to the published version of the manuscript.

Funding: This research was funded by National Natural Science Foundation of China (52375201) and Project for Science and Technology Plan of Henan Province (262102220037).

Data Availability Statement: The original contributions presented in this study are included in the article. Further inquiries can be directed to the corresponding author(s).

Conflicts of Interest: Author Lexia Wei was employed by the company Liuzhou Wuling New Energy Automobile Co., Ltd. The remaining authors declare that the research was conducted in the absence of any commercial or financial relationships that could be construed as a potential conflict of interest.

References

1. Zhang, Y.; Wei, S.; Yang, W.; Guan, J.; Li, G. Study on the Wear Performance of 20CrMnTi Gear Steel with Different Penetration Gradient Positions. *Materials* **2025**, *18*, 3685. [CrossRef] [PubMed]
2. Holmberg, K.; Erdemir, A. Influence of Tribology on Global Energy Consumption, Costs and Emissions. *Friction* **2017**, *5*, 263–284. [CrossRef]
3. Li, Y.; Cheng, G.G.; Lu, J.L.; Sun, J. The Effect of TiN Precipitated Particles on the Austenite Grain and Hardenability of 20CrMnTi Gear Steel. *Ironmak. Steelmak.* **2022**, *49*, 1004–1013. [CrossRef]
4. Tang, J.; Hu, X.; Lai, F.; Guo, X.; Qu, S.; He, R.; Qin, S.; Li, J. Evolution of Fretting Wear Behaviors and Mechanisms of 20CrMnTi Steel after Carburizing Treatment. *Metals* **2020**, *10*, 179. [CrossRef]
5. Wang, L.; Yang, L.; Wang, L.; Tang, X.; Liu, G. Influence Mechanism of Grinding Surface Quality of 20CrMnTi Steel on Contact Failure. *Sci. Rep.* **2024**, *14*, 13374. [CrossRef] [PubMed]
6. Kong, W.; Zhang, D.; Tao, Q.; Chen, K.; Wang, J.; Wang, S. Wear properties of the deep gradient wear-resistant layer applied to 20CrMnTi gear steel. *Wear* **2019**, *424–425*, 216–222. [CrossRef]
7. Braumann, L.; Sáenz de Viteri, V.; Morhard, B.; Lohner, T.; Ochoa, J.; Amri, H. Tribology Technologies for Gears in Loss of Lubrication Conditions: A Review. *J. Mater. Sci. Mater. Eng.* **2025**, *20*, 29. [CrossRef]
8. Akama, M. Rolling Contact Fatigue and Wear of Rails and Wheels: A Comprehensive Review. *Machines* **2025**, *13*, 970. [CrossRef]
9. Oila, A.; Bull, S.J. Assessment of the Factors Influencing Micropitting in Rolling/Sliding Contacts. *Wear* **2005**, *258*, 1510–1524. [CrossRef]
10. Yin, H.; Wu, Y.; Liu, D.; Zhang, P.; Zhang, G.; Fu, H. Rolling Contact Fatigue-Related Microstructural Alterations in Bearing Steels: A Brief Review. *Metals* **2022**, *12*, 910. [CrossRef]
11. Sadeghi, F.; Jalalahmadi, B.; Slack, T.S.; Raje, N.; Arakere, N.K. A Review of Rolling Contact Fatigue. *J. Tribol.* **2009**, *131*, 041403. [CrossRef]
12. Yang, Q.X.; Ren, X.J.; Zhao, Y.H.; Gao, Y.K.; Li, Y.L.; Yao, M. Effect of Carburization on Residual Stress Field of 20CrMnTi Specimen and Its Numerical Simulation. *Mater. Sci. Eng. A* **2005**, *392*, 240–247. [CrossRef]
13. Wang, H.; Yi, Y.; Wang, G.; Zhao, X.; Yin, F. Effect of Ultrasonic Shot Peening Pretreatment on Carburizing Heat Treatment Process of 20CrMnTi Gear Steel. *ACS Appl. Mater. Interfaces* **2025**, *17*, 25934–25950. [CrossRef] [PubMed]
14. Lei, Z.; Li, Z.; Xiao, Y. Comparative Tribological Performance of a-C:H, ta-C and AlCrSiN Coatings on 20CrMnTi Gear Steel under Dry Sliding Condition. *Ind. Lubr. Tribol.* **2023**, *75*, 1125–1137. [CrossRef]
15. Hu, H.; Shi, X.; Wu, C.; Zhai, W.; Liu, X.; Qin, H.; Chen, Y.; Huang, Q. Recent Advances in Metal Additive Manufacturing from a Tribological Perspective. *J. Alloys Compd.* **2025**, *1050*, 185613. [CrossRef]
16. Neville, A.; Morina, A.; Haque, T.; Voong, M. Compatibility between Tribological Surfaces and Lubricant Additives—How Friction and Wear Reduction Can Be Controlled by Surface/Lube Synergies. *Tribol. Int.* **2007**, *40*, 1680–1695. [CrossRef]
17. Cai, Y.; Aslam, J.; Xue, J.; Song, Q.; Ma, H.; Liu, Z. Enhancement of Tribological Performance with Laser Surface Texturing: A Review. *Proc. Inst. Mech. Eng. Part J J. Eng. Tribol.* **2025**, *239*, 1291–1312. [CrossRef]
18. Chen, K.; Tang, Y. Research Progress on the Design of Surface Texture in Tribological Applications: A Mini-Review. *Symmetry* **2024**, *16*, 1523. [CrossRef]
19. Huang, Q.; Shi, X.; Xue, Y.; Zhang, K.; Wu, C. Recent Progress on Surface Texturing and Solid Lubricants in Tribology: Designs, Properties, and Mechanisms. *Mater. Today Commun.* **2023**, *35*, 105854. [CrossRef]
20. Dias, L.C.; Pintaude, G.; Vittorino, A.A.O.F.; Costa, H.L. ZDDP Tribofilm Formation from a Formulated Oil on Textured Cylinder Liners. *Lubricants* **2022**, *10*, 118. [CrossRef]
21. Qin, H.; Shi, X.; Wu, C.; Chen, Y.; Hu, H.; Huang, Q. Bioinspired Surface Texturing: From Natural Prototypes to Advanced Applications and Future perspectives. *J. Bionic Eng.* **2026**, *23*, 1991–2023. [CrossRef]
22. Sheng, Z.; Zhu, H.; He, Y.; Shao, B.; Sheng, Z.; Wang, S. Tribological Effects of Surface Biomimetic Micro–Nano Textures on Metal Cutting Tools: A Review. *Biomimetics* **2025**, *10*, 283. [CrossRef] [PubMed]
23. Mzali, S.; Elwasli, F.; Mezlini, S.; Hajlaoui, K.; Alrasheedi, N.H. Tribological Behavior of 3D Printed Biomimetic Surfaces. *Tribol. Int.* **2024**, *193*, 109352. [CrossRef]
24. Bhushan, B. Biomimetics: Lessons from Nature—An Overview. *Philos. Trans. R. Soc. A* **2009**, *367*, 1445–1486. [CrossRef] [PubMed]

25. Hazel, J.; Stone, M.; Grace, M.S.; Tsukruk, V.V. Nanoscale Design of Snake Skin for Reptation Locomotions via Friction Anisotropy. *Biomacromolecules* **1999**, *32*, 477–484. [CrossRef] [PubMed]
26. Abdel-Aal, H.A. On Surface Structure and Friction Regulation in Reptilian Limbless Locomotion. *J. Mech. Behav. Biomed. Mater.* **2013**, *22*, 115–135. [CrossRef] [PubMed]
27. Liu, Y.; Zhu, Q.; Wang, C.; Li, J. Tribological Behavior of CoCrMo Artificial Knee Joint with Symmetrically Biomimetic Textured Surfaces on PEEK. *Opt. Laser Technol.* **2023**, *157*, 108774. [CrossRef]
28. Acar, Ç.G.; Žunda, A. Tribological Aspects of Graphene and Its Derivatives. *Lubricants* **2025**, *13*, 232. [CrossRef]
29. Lin, H.; Zhai, W.; Li, Z.; Wang, M.; Chen, Q.; Zhou, R.; Fu, Y.; Huang, J.; Liu, M.; Zhao, G.; et al. Enhanced Fabrication and Microstructure-property Optimization of IN718 Superalloy via Laser Rolling-assisted Wire-arc Directed Energy Deposition. *Mat. Sci. Eng. A-Struct.* **2025**, *944*, 148890. [CrossRef]
30. Ayerdi, J.J.; Aginagalde, A.; Llavori, I.; Bonse, J.; Spaltmann, D.; Zabala, A. Ball-on-flat Linear Reciprocating Tests: Critical Assessment of Wear Volume Determination Methods and Suggested Improvements for ASTM D7755 Standard. *Wear* **2021**, *470*, 203620. [CrossRef]
31. Archard, J.F. Contact and Rubbing of Flat Surfaces. *J. Appl. Phys.* **1953**, *24*, 981–988. [CrossRef]
32. Vetter, J. 60 Years of DLC Coatings: Historical Highlights and Technical Review of Cathodic Arc Processes to Synthesize Various DLC Types, and Their Evolution for Industrial Applications. *Surf. Coat. Technol.* **2014**, *257*, 213–240. [CrossRef]
33. Gachot, C.; Rosenkranz, A.; Hsu, S.M.; Costa, H.L. A Critical Assessment of Surface Texturing for Friction and Wear Improvement. *Wear* **2017**, *372–373*, 21–41. [CrossRef]
34. Rosenkranz, A.; Reinert, L.; Gachot, C.; Mücklich, F. Alignment and Wear Debris Effects between Laser-Patterned Steel Surfaces under Dry Sliding Conditions. *Wear* **2014**, *318*, 49–61. [CrossRef]
35. Li, Z.; Guan, X.; Wang, Y.; Li, J.; Cheng, X.; Lu, X.; Wang, L.; Xue, Q. Comparative Study on the Load Carrying Capacities of DLC, GLC and CrN Coatings under Sliding-Friction Condition in Different Environments. *Surf. Coat. Technol.* **2017**, *321*, 350–357. [CrossRef]
36. Duminica, F.D.; Belchi, R.; Libralesso, L.; Mercier, D. Investigation of Cr(N)/DLC Multilayer Coatings Elaborated by PVD for High Wear Resistance and Low Friction Applications. *Surf. Coat. Technol.* **2018**, *337*, 396–403. [CrossRef]
37. Rosenkranz, A.; Pangraz, J.C.; Gachot, C.; Mücklich, F. Load-Dependent Run-In and Wear Behaviour of Line-Like Surface Patterns Produced by Direct Laser Interference Patterning. *Wear* **2016**, *368–369*, 350–357. [CrossRef]

Disclaimer/Publisher's Note: The statements, opinions and data contained in all publications are solely those of the individual author(s) and contributor(s) and not of MDPI and/or the editor(s). MDPI and/or the editor(s) disclaim responsibility for any injury to people or property resulting from any ideas, methods, instructions or products referred to in the content.